RSC Advances

PAPER

View Article Online
View Journal | View Issue

Cite this: *RSC Adv.*, 2024, **14**, 15058

Application of static integrated skeletal reduction and tabulation of dynamic adaptive chemistry in the combustion simulation of ethylene-fueled scramjet combustor†

Zhongwen Li,[ab] Jianwen Liu[c] and Jingbo Wang *[ab]

The high-fidelity reduced mechanism is one of the key elements in the combustion simulation of scramjet combustors to reveal their combustion and flow phenomena. In the present work, the hierarchically constructed NUIGMech1.2 (2857 species and 11 814 reactions) is applied to the combustion simulation of an ethylene-fueled scramjet combustor using the method of static integrated skeletal reduction and tabulation of dynamic adaptive chemistry (TDAC). The integrated skeletal reduction strategy successively consists of species elimination using the revised directed relation graph with error propagation method of fixed species scheme and improved sensitivity analysis method, and reactions elimination based on computational singular perturbation importance index. A preferred ethylene skeletal mechanism (26 species and 117 reactions) is obtained through the integrated skeletal reduction strategy under target working conditions of temperature range of 900–1800 K, pressure range of 1–4 atm, and equivalence ratio range of 0.25–5.0. The compact skeletal mechanism is comprehensively validated against the experimental results of ignition delay times, laminar flame speeds, and key species concentration profiles. Meanwhile, it shows consistent results with the detailed mechanism on the adiabatic flame temperature profiles and "S"-curves. When applying this skeletal mechanism to combustion simulations of ethylene-fueled scramjet combustor with double parallel cavities, the path flux analysis method and *in situ* adaptive tabulation algorithm of TDAC is further utilized to speed up the chemical reaction solution process at run-time. Under the scramjet and ramjet modes, the corresponding simulation results in terms of flame luminosity images, schlieren images, and static pressure distributions, coincide well with those of experimental measurements. The combustion and flow characteristics of the two modes are investigated and analyzed comparatively based on above results and combustion performance parameters. Present work contributes to the application of fuel kinetic mechanisms in scramjet combustor combustion simulation.

Received 29th January 2024
Accepted 5th April 2024

DOI: 10.1039/d4ra00749b

rsc.li/rsc-advances

1. Introduction

Ethylene (C_2H_4) has the advantages of easy storage, short ignition delay time, and great energy per unit volume, which is also an important intermediate during oxidation and pyrolysis process of large hydrocarbons.[1–5] Thus, it serves as fuel or surrogate fuel in practical scramjet combustors.[3,6–11] Ethylene kinetic mechanism with high accuracy is one of the key elements for combustion simulation of ethylene-fueled scramjet combustors to reveal their combustion and flow phenomena.

Global mechanisms of one step reaction[12,13] or several steps of reactions with hydrogen (H_2) and carbon monoxide (CO) as intermediates[14–16] were adopted in previous combustion simulations of scramjet combustors.[6,13,16–18] Due to the lack of universality of this kind of mechanisms, the prediction results gained are unsatisfactory under some circumstances,[17,19] and the relevant combustion phenomena like flame propagation and dynamic evolution of combustion processes cannot be explained reasonably.[20,21] Furthermore, they predict mostly incorrect trends or even fail to be solved in predicting fuel characteristics in kinetic simulations.[20,22] In recent decades, a variety of detailed kinetic models related to ethylene–air combustion are developed.[23–38] Among them, the NUIGMech1.2,[38] including 2857 species and 11 814 reactions, is hierarchically constructed that well characterize the combustion and pyrolysis characteristics for fuels ranging from C_0–C_7 hydrocarbons[35,36,38–41] under wide working conditions. In terms

[a]School of Chemical Engineering, Sichuan University, Chengdu, 610065, P. R. China. E-mail: wangjingbo@scu.edu.cn
[b]Engineering Research Center of Combustion and Cooling for Aerospace Power, Ministry of Education, Sichuan University, Chengdu, 610065, P. R. China
[c]Beijing Power Machinery Institute, Beijing, 100074, P. R. China

† Electronic supplementary information (ESI) available. See DOI: https://doi.org/10.1039/d4ra00749b

of chemical kinetics, these mechanisms are good in predicting the characteristics of ethylene combustion. However, their large size leads to high computational cost when solving the corresponding chemical source terms and brings stiff problem to numerical solution.[42,43] Thus, they cannot be directly applied to computationally expensive combustion simulation for ethylene-fueled scramjet combustors.

To facilitate the application of fuel mechanisms in combustion simulation of combustors, many mechanism reduction methods including skeletal reduction, lumping, time-scale analysis, *etc.*, are developed in recent years to obtain skeletal mechanism without sacrificing accuracy on relevant combustion characteristics within a certain range of working conditions.[42,44] Skeletal reduction as the main reduction method eliminates unnecessary species and reactions by dealing with complex coupling between species or reactions.[42,44] Lu *et al.*[45] first proposed the directed relation graph (DRG) method, and then a series of derivative methods including revised-DRG (r-DRG),[46] DRG with error propagation (DRGEP),[47] revised-DRGEP (r-DRGEP),[44] path flux analysis (PFA),[48] linearized error propagation (LEP),[49] *etc.*, are successively developed. Sensitivity analysis (SA) based methods are created later to aid reduction process, which eliminate unnecessary species by performing sensitivity analyses on certain retained species set. Given these methods are computationally expensive, they are often combined with DRG-related methods, and the corresponding methods include DRGASA,[50] DRGEPASA[51] and ISASA.[52] Xue *et al.*[44] recently proposed a fixed species (FS) scheme for six DRG-related methods to retain the species increasing the maximum error of ignition delay time sharply in skeletal reduction processes. The r-DRGEP method with the FS scheme showed good performance in the reduction of AramcoMech3.0 [33] for fourteen C_0–C_4 hydrocarbon and oxygenated fuels. Xi *et al.*[53] improved SA method by introducing the scheme of recognition of strongly coupled species pairs and incremental deletion. As demonstrated in the reduction of *n*-heptane mechanism, the computational cost is greatly decreased compared with the traditional SA method. Moreover, reaction elimination methods for skeletal reduction are also developed, like elementary flux analysis (EFA)[54] method and reaction elimination based on the computational singular perturbation (CSP) importance index.[55] Lumping method is also introduced to reduce the mechanism size by combining similar species and reaction pathways.[42] Although time-scale analysis reduction, such as quasi steady state approximation (QSSA),[56,57] CSP,[58] *etc.*, can significantly reduce the mechanism size, the derived mechanism lacks universality for applications in customized or commercial software as reactions are not expressed in the extended Arrhenius format.[59] In view of each reduction method is tailored for a certain reduction stage, integrated strategies are preferred in mechanism reduction process, which are proved to be reliable and efficient to achieve maximal reduction of many fuels.[11,55,59]

Considering the application of reduction methods to the detailed mechanisms of ethylene, some skeletal mechanisms obtained under specific reduction conditions are summarized in Table 1. As for the detailed mechanisms adopted for reduction, Laskin Mech,[23] USC-II,[28] LLNL Mech[24] and UCSD[32] focus more on high temperature combustion of small hydrocarbons.[34] GRI-Mech 3.0 [25] is mainly optimized for natural gas combustion. Therefore, these mechanisms are not well suited for wide conditions of ethylene combustion in combustion simulation of scramjet combustor. Different combustion characteristics can be as reduction target, such as ignition delay time (IDT), laminar flame speed (LFS), "S"-curve,[60] the ignition characteristics deserve more attentions than other kinetics properties for scramjet combustors.[4] Under narrow reduction conditions of single temperature and pressure point (298 K, 1 atm), a compact ethylene skeletal mechanism 23S–55R was obtained with an integrated reduction strategy. However, under wide temperature range of 800–1600 K, a larger skeletal mechanism 70S–451R was obtained by the single reduction method of DRGEP with FS scheme. Given the wide range of temperature, pressure, and equivalence ratio for scramjet combustor, there is still lack of a compact and comprehensively validated ethylene skeletal mechanism suitable for combustion simulation of scramjet combustors.

The tabulation of dynamic adaptive chemistry (TDAC) method is proved to be a promising method to utilize skeletal or detailed mechanisms in combustion simulation of combustors.[66–69] The TDAC method[66] reduce prohibitive computational cost in the solution of species transport equations by coupling *in situ* adaptive tabulation algorithm (ISAT)[70] and dynamic adaptive chemistry (DAC).[71] The ISAT algorithm decreases the effect of the number of cells by tabulating and reusing previously solutions, whereas the DAC method decreases the effect of the mechanism size by acquiring local reduced mechanisms at run-time.[66–68] Preliminary static reduction of detailed mechanisms before applying DAC or TDAC method can dramatically decrease computational cost and storage requirements while guaranteeing accuracy and good acceleration performance.[67,68,71,72] Li *et al.*[67] evaluated the speed-up performance of different dynamic reduction methods (DRG, DRGEP, DAC, PFA, and EFA) with ISAT turned on for skeletal and detailed mechanisms of natural gas and biogas in combustion simulation of Delft jet in hot co-flow (DJHC) burner, and found that PFA provides a slightly larger speed-up factor for skeletal mechanism.

Considering the extensive applications of ethylene as fuel or surrogate fuel and the lack of its skeletal mechanism with high-fidelity applicable for wide range of operating conditions of scramjet combustors, present work aims to obtain a compact and comprehensively validated ethylene skeletal mechanism based on the development of ethylene mechanisms and newly proposed mechanism reduction methods. A static integrated skeletal reduction is performed for the high accuracy NUIG-Mech1.2 [38] containing ethylene sub-mechanism to obtain a preferred skeletal mechanism under target operating conditions. After systematic kinetic verifications for reliability on the skeletal mechanism, it is applied to the combustion simulations of an ethylene-fueled scramjet combustor combined with the TDAC method.[66] And then the flow and combustion characteristics under a scramjet and a ramjet operating modes are

Table 1 Some representative ethylene skeletal mechanisms recently obtained by reduction of detailed mechanisms for specific working conditions

Detailed mechanism	Target	Reduction method	Reduction conditions[a]	Skeletal mechanism[b]
Laskin Mech[23]	—	DRGEPSA	T: 1100–1500 K p: 1 atm Φ: 1.0	25S–131R[61]
GRI-Mech 3.0 [25]	—	DRG CSP importance index	T: 1300–1700 K p: 1 atm Φ: 0.4–1.4	19S–32R[62]
UCSD[32]	IDT	DRGEP SA CSP	T: 1000–1800 K p: 1.0–5.0 atm Φ: 0.5–1.5	24S–86R[11]
USC-II[28]	IDT	DRG	T: 1200–1800 K p: 1–3 atm Φ: 0.6–1.4	38S–230R[63]
LLNL Mech[24]	LFS	DRGEP QSSA SA	T: 298 K p: 1 atm Φ: 0.6–1.2	23S–55R[64]
USC-II[28]	"S"-curve	LEP	T: 1000 − (adiabatic flame temperature − 100) K p: 0.5–10 atm Φ: 0.5–1.5	35S–228R[49]
AramcoMech 3.0 [33]	IDT	DRGEP with FS	T: 800–1600 K p: 1–10 atm Φ: 0.5–1.5	70S–451R[44]
USC-II[28]	IDT	PFA modified SA	T: 1500–2500 K p: 20–60 atm Φ: 0.5–1.5	26S–55R[65]

[a] Symbol T, p, and Φ respectively mean temperature, pressure, and equivalence ratio for reduction conditions. [b] Labelled by the number of species and reactions in the corresponding skeletal mechanism.

investigated according to the results of combustion simulations and the discussion of combustion performance parameters.

2. Computational specifications

2.1. Static reduction setup

The flowchart of the static integrated reduction with NUIG-Mech1.2 [38] as the detailed mechanism is illustrated in Fig. 1. Mechanism extraction and clean-up is first carried out to extract sub-mechanism of species with carbon number ≤4 (including H_2 mechanism) and clean unnecessary sub-mechanisms of NO_x and NH_3. According to the operating conditions of the ethylene-fueled scramjet combustor,[3,5,10,11,22,73] the temperature range of 900–1800 K, pressure range of 1–4 atm, and equivalence ratio range of 0.25–5.0 are chosen as the reduction conditions. The cost-effective r-DRGEP with FS method[44] and the efficient but slightly expensive improved SA method[53] are employed to perform the two stage species eliminations, followed by the reactions elimination based on the method of CSP importance index.[55] Systematic kinetic verifications are conducted on the preferred skeletal mechanism intended for combustion simulation to check its reliability. These verifications, including ignition delay times (IDTs), laminar flame speeds (LFSs), species concentration profiles (SCPs), adiabatic flame temperature profiles (AFTPs) and "S"-curves, are performed by the Chemkin-pro package.[74] Present integrated skeletal reduction is performed by the automatic mechanism reduction program ReaxRed[44,75] adopting the relative error of IDTs as the indicator, which has proven to be effective in extensive reduction practices.[44,53,55,76,77]

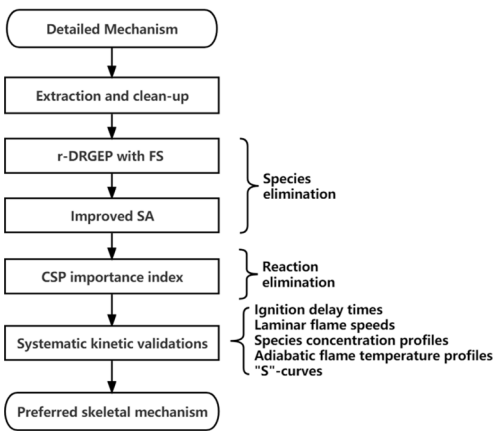

Fig. 1 The integrated skeletal reduction strategy.

2.2. Computational domain and boundary conditions

The structure and experimental measurement data of investigated model scramjet combustor are taken from the researches of Zhong *et al.*[3,10] As shown in Fig. 2(a), the scramjet combustor consists of an isolator section of 674 mm in length (equal-area of 75 mm × 54.5 mm), and three unilaterally diverging combustor sections with lengths of 480 mm, 702 mm, and 344 mm, respectively. The divergence angles are 2.5°, 3.5°, and 4° in

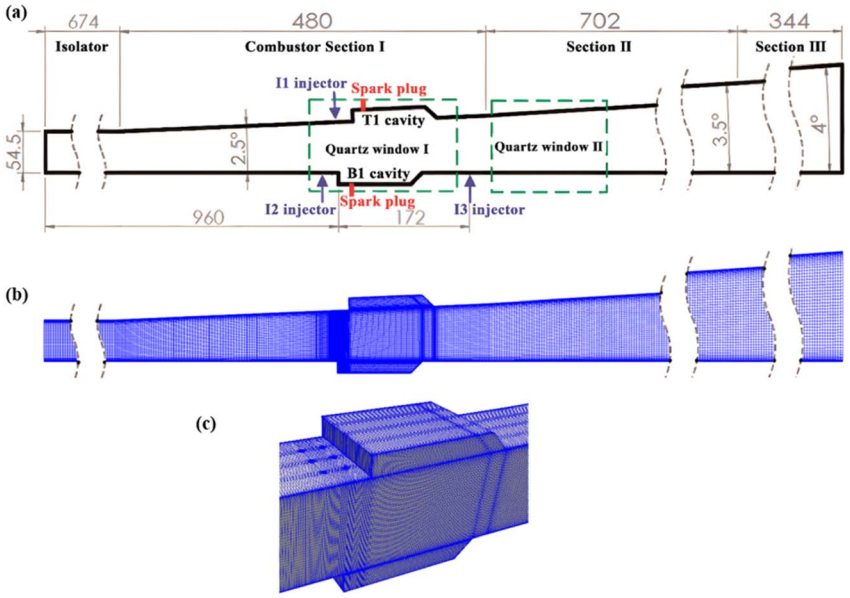

Fig. 2 (a) The schematic diagram of scramjet combustor[10] (unit in mm); (b) Ooverall computational mesh; (c) mesh refinement around integrated fuel-injection/flame-holder cavity modules.

sequence. Two integrated fuel-injection/flame-holder cavity modules are installed on the upper and lower walls of combustor Section I. The fuel-injection part is located 8 mm upstream of the leading edge of the cavity and has three 2.0 mm diameter holes symmetrically spaced 18 mm apart. The depth, length, width, and aft ramp angle of flame-holder cavity are respectively 15 mm, 110 mm, 75 mm, and 45°. For more details on the combustor configuration, the experimental setup and data measurements please refer to the experimental researches.[3,10] According to the mesh independent analysis in ESI,† the hexahedral structured mesh containing approximately 4.89 million cells is utilized to discrete the computational domain, as illustrated in Fig. 2(b) and (c). The outer and inner O grid block schemes are adopted for six ethylene jet holes, and the cells are clustered towards shear layers of cavities and downstream of the ethylene jets.

The total temperature T_0, total pressure p_0, and Mach number Ma of the vitiated air at combustor inlet is about 1430 K, 3.6 MPa, and 3.46. The ethylene injection pressure of injectors I1 and I2 are used to adjust the global equivalence ratio to perform a series of combustion experimental studies and there is a certain degree of fluctuations in the injection pressure of the ethylene jets.[10] In the present work, combustion simulations are performed for two typical operating conditions with relatively comprehensive experimental data belonging to a scramjet ($\Phi = 0.26$) and a ramjet ($\Phi = 0.51$) operating mode.[10] Their mode classifications are based on the quasi-one-dimensional (1-D) data analysis method.[78] The flow parameters and components (in mass fraction) of the vitiated air and fuel jets prescribed under the two modes are summarized in Table 2. The turbulent intensities I of vitiated air and ethylene jets are taken as 1% and 5%. The turbulent kinetic energy k and specific dissipation rate ω are respectively estimated by $1.5(UI)^2$ and $k^{0.5}/(C_\mu^{0.25}l)$, where U is the magnitude of velocity and constant C_μ equals to 0.09. Turbulent length scale l is calculated by $0.07L$, where the relevant dimension L are the diameter of the injector for ethylene jets and the hydraulic diameter for combustor inlet. Wall functions of kqRWallFunction, omegaWallFunction, alphatWallFunction, and nutkWallFunction are adopted and targeted for high Reynolds number flow to model corresponding turbulence variables in boundary layers.

2.3. Numerical simulation setup

The combustion simulations are carried out using the high speed gas phase compressible combustion solver[79] developed on the open-source platform OpenFOAM.[80] The inviscid convective fluxes are evaluated by Kurganov and Tadmor (KT) scheme[81,82] that considers the wave transmission speed based on the central scheme, and determines a smaller dissipation coefficient according to the wave speed. Second-order backward

Table 2 Flow parameters and components of vitiated air and ethylene fuel jets for the two operating modes

Parameter	Vitiated air	Scramjet mode	Ramjet mode
Φ	—	0.26	0.51
T_0 [K]	1430	305	305
T [K]	485.68	272.37	272.37
p_0 [Pa]	3.60×10^6	1.06×10^6	2.05×10^6
p [Pa]	4.00×10^4	5.90×10^5	1.14×10^6
Ma	3.46	1.00	1.00
U [m s^{-1}]	1491.29	316.30	316.30
Y_{O_2}	0.2495	0.00	0.00
Y_{H_2O}	0.0356	0.00	0.00
Y_{CO_2}	0.1414	0.00	0.00
Y_{N_2}	0.5735	0.00	0.00
$Y_{C_2H_4}$	0.00	1.00	1.00

time integration scheme is used.[83] Second-order total variation decreasing scheme (van Leer flux limiter[84]) is used for divergence schemes of velocity, species mass fraction, internal energy, and turbulence variable fluxes. Laplacian schemes are Gauss linear corrected and the surface normal gradient scheme is corrected. The gradient schemes of turbulence variables, velocity, and pressure are cellLimited Gauss Linear 1, and the others are Gauss linear by default. The interpolation scheme for the reconstructed density, velocity, temperature, and species mass fraction is van Leer and the others are linear by default. Ignition in simulation is accomplished by means of adding energy source terms in the patch region over a period. Adjustable time step is used and the maximum Courant–Friedrichs–Lewy (CFL) number is set to 0.3. Turbulent Schmidt number Sc_t and turbulent Prandtl number Pr_t are respectively set to 0.9 and 0.72.

The SST k–ω turbulence model[85–87] and the partially stirred reactor (PaSR) combustion model[88–90] are respectively used to model turbulent flow, turbulence and combustion interaction. The model constant C_{mix} in PaSR is taken as 0.01.[16,22] The mechanism reduction method for TDAC part is PFA reduction method[48,67] and ISAT algorithm.[70] On the TDAC reduction, the ISAT tabulation tolerance ε_{ISAT} and the reduction tolerance ε_{PFA} are both set to 1×10^{-4} according to previous related studies.[66–68] Previous studies indicated that thermal radiation can affect the combustion characteristics of premixed combustible mixtures in one-dimensional laminar burning velocity.[91,92] Whereas the radiation effect is usually ignored in the combustion simulations in engineering scale scramjet combustors,[17,22,73,93] and therefore its effect is not considered in current simulations.

3. Results and discussions

3.1. Acquisition of preferred skeletal mechanism and its systematic kinetic verifications

Following the scheduled strategy in Fig. 1, the skeletal reduction is carried out for NUIGMech1.2 by setting the maximum relative error (MaxRE) of IDTs ≤20% [34] under the target reduction conditions. The ethylene skeletal mechanisms obtained at different stages are summarized in Table 3. After the first stage of species eliminations using r-DRGEP with FS scheme,[44] the obtained skeletal mechanism 44S–217R is significantly reduced compared to the pre-processed mechanism 581S–3200R. A more compact skeletal mechanism 26S–153R is derived in the second stage reduction for uncertain species set by adopting the improved SA method[53] with a slight increase in the mean relative error (MeanRE) of IDTs from 5.07% to 6.40%. After elimination of unimportant reactions based on the method of CSP importance index,[55] the skeletal mechanism 26S–117R is obtained with the MeanRE of 7.16%. Given its compact size and the ability to predict IDTs within reasonable accuracy,[34] the mechanism 26S–117R is chosen as the preferred skeletal mechanism. Its comprehensive kinetic verifications concerning IDTs, LFSs, SCPs, *etc.* under the present reduction conditions are respectively shown in Fig. 3–7. Furthermore, considering the mechanisms applicable for ethylene combustion, such as mechanisms of 24S–86R,[11] 35S–228R,[49] 38S–230R,[63] and 70S–451R[44] in Table 1, their kinetic performances are systematically compared with the preferred skeletal mechanism obtained in present work in the ESI.† Compared to these mechanisms, the preferred skeletal mechanism has the advantages of favourable prediction results and compact in size.

Auto-ignition of fuel accounts for flame stabilization mechanism in combustion simulations of scramjet combustors,[94,95] so the ability to accurately predict IDTs is an important aspect of high-fidelity skeletal mechanism.[4] The ignition data for wide range conditions of ethylene/air mixtures in a shock tube was recently supplemented by Yang *et al.*[34] The relevant experimental data and simulation settings are adopted in present work to show the performance of the skeletal mechanism. As illustrated in Fig. 3, the skeletal mechanism well reproduces the simulation results of the detailed mechanism under various conditions, and its prediction results match well with the experimental data. The pressure effect and the two cross-effects[34,96,97] under lean-burn conditions are accurately captured by the skeletal mechanism.

Although the diffusion process is one or more orders of magnitude slower than the fluid-dynamic time scales at high speed situation, the residence time can be distinctly longer in recirculation zone (Ma ≈ 0) formed by flameholder, hence the accurate prediction of LFSs becomes significant for the skeletal mechanism.[4] Fig. 4 displays the simulation results of LFSs of the skeletal and the detailed mechanism for ethylene/air mixtures under various equivalence ratios. Under the conditions of 298 K with initial pressures of 1 and 2 atm, the skeletal mechanism gives slightly larger simulation results than those of detailed mechanism. As shown in Fig. 4(b), the skeletal mechanism improves the insufficient prediction of the detailed mechanism under the conditions of 1 atm with initial temperatures of 298, 360 and 470 K, and the corresponding results are more in line with experimental data. Overall, the skeletal

Table 3 Skeletal mechanisms obtained in different static reduction stages

Methods	Skeletal mechanisms	MaxRE[a]	MeanRE[a]
Extraction and clean-up	581S–3200R	—	—
r-DRGEP with FS	44S–217R	16.24%	5.07%
r-DRGEP with FS + improved SA	26S–153R	14.94%	6.40%
r-DRGEP with FS + improved SA + CSP importance index	26S–117R	16.19%	7.16%

[a] Maximum relative error and mean relative error under the reduction conditions.

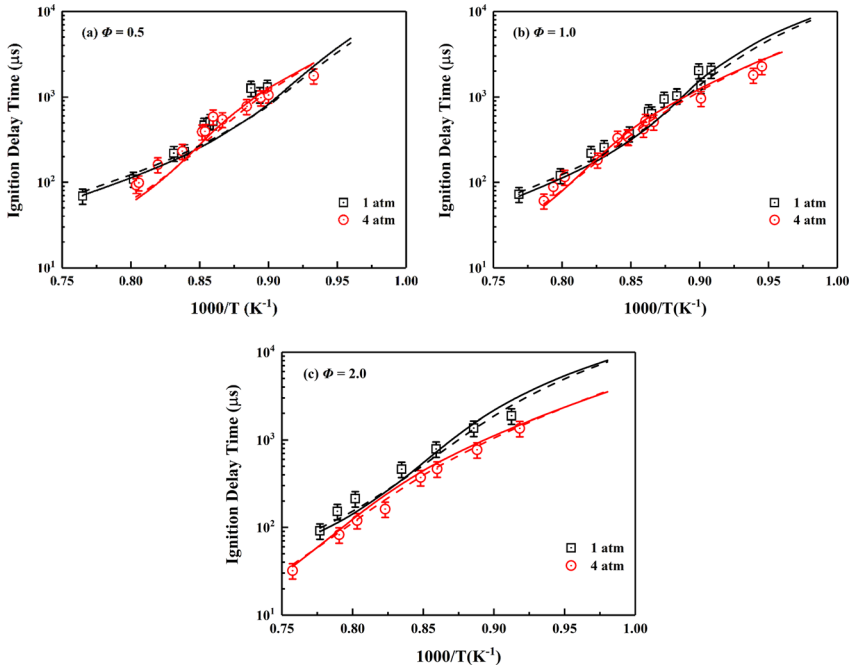

Fig. 3 Validation of IDTs of ethylene/air mixture for the skeletal mechanism under the wide temperature, pressures of 1, 4 atm and different equivalence ratios. Symbols are experimental data;[34] solid lines are predictions using the skeletal mechanism; dashed lines are predictions using NUIGMech1.2.

mechanism captures the pressure and temperature effect under the tested conditions.

The SCPs obtained in a jet-stirred reactor (JSR) characterize the evolution process on the consumption and production of interested species under operating conditions. Jallais *et al.* conducted JSR experiments on the oxidation of ethylene under various conditions (T = 773–900 K, p = 1.0 atm, and Φ = 3, 5, and 10).[104] The initial mole fraction is 0.05 for ethylene diluted by N_2, and the residence time is 1.3 s. The simulated concentration profiles of fuel (C_2H_4), and major products (CO, CO_2) against experimental data in ethylene oxidation at different equivalence ratios are shown in Fig. 5. From the comparison results, the conclusion can be safely drawn that the skeletal mechanism presents good prediction for fuel consumption and major products generation in ethylene oxidation process.

AFTPs are of paramount importance to characterize the stable combustion region when analysing premixed flames.[105,106] Fig. 6 shows the comparison of AFTPs at equivalence ratio rang of 0.1–4.0 under initial temperature of 1000 K and pressures of 1.0 and 4.0 atm. The initial temperature is determined by the non-reactive temperature field adjacent to the two cavities with fuel injected, and the fuel and oxidizer are respectively ethylene and the vitiated air mentioned in Table 1. The obtained AFTPs are basically indistinguishable, which verifies the reliability of the thermochemical characteristics.

"S"-curve characterizes the variation of combustion state of premixed mixture in perfectly stirred reactor (PSR) with residence time.[49,60] For the large span of residence time for scramjet combustor combustion conditions,[22] the skeletal mechanism should maintain the prediction performance of the detailed mechanism on the combustion state of ignition, extinction,

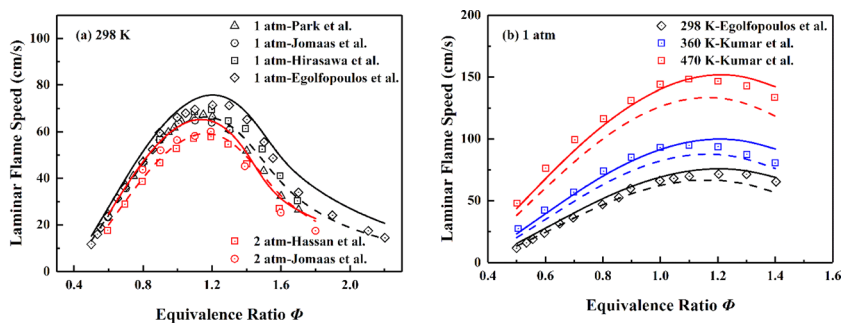

Fig. 4 Validation of LFSs of ethylene/air mixture of various equivalence ratios at different initial pressures and temperatures. Symbols are experimental data;[98–103] solid lines are predictions using the skeletal mechanism; dashed lines are predictions using NUIGMech1.2.

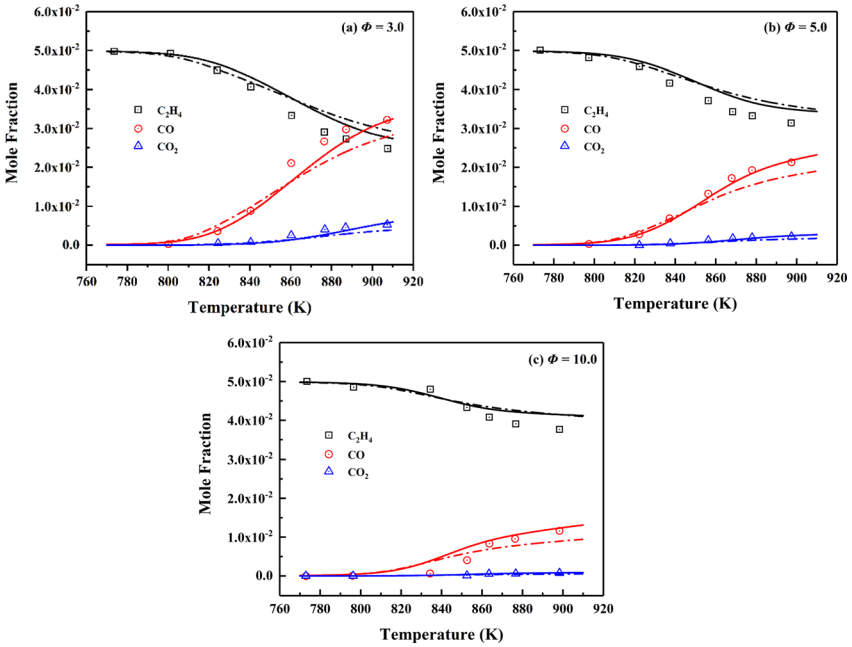

Fig. 5 Validation of SCPs of fuel and major products for $C_2H_4/O_2/N_2$ mixtures of different equivalence ratios at the pressure of 1.0 atm and temperature range of 773–900 K. Symbols are experimental data;[104] solid lines are predictions using the skeletal mechanism; dashed lines are predictions using NUIGMech1.2.

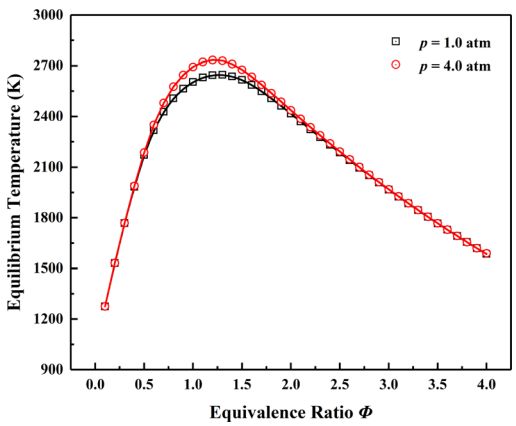

Fig. 6 AFTPs of ethylene/vitiated air mixture of different equivalence ratios under temperature of 1000 K and pressures of 1.0 and 4.0 atm. Symbols are prediction using NUIGMech1.2; solid lines are prediction using the skeletal mechanism.

intermediate unstable combustion, and stable combustion of premixed mixture. Fig. 7 presents the simulation results of "S"-curves simulated by the detailed and the skeletal mechanism at equivalence ratios of 0.5, 1.0 and 2.0 and pressures of 1 and 4 atm. Same to the simulation setting in AFTPs, the fuel and oxidizer are respectively ethylene and the vitiated air, and the initial temperature of PSR is 1000 K. The skeletal mechanism accurately captures important combustion state of premixed mixture of different equivalence ratios and pressures in combustion process.

According to above systematic kinetic verifications, the simulation results of the skeletal mechanism are in good agreement with the experimental measurements for IDTs, LFSs, and SCPs. Meanwhile, it provides consistent results with the detailed mechanism in the aspects of AFTPs and "S"-curves. Additionally, reaction path analyses of the detailed mechanism and the skeletal mechanism for the ignition moments relevant to combustion conditions are provided in ESI.† As can be concluded from the analysis results, the preferred skeletal mechanism retains dominant key reaction pathways of ethylene combustion processes. Therefore, this compact and high-fidelity skeletal mechanism is well prepared for the combustion simulations of scramjet combustor in the subsequent section.

3.2. Application of the skeletal mechanism in combustion simulations

With the customized solver developed on OpenFOAM platform,[79] the comparison of the computational efficiencies of the skeletal mechanisms of 44S–217R *versus* 26S–117R is carried out under other identical setups for combustion simulations. For the commonly adopted direct stiff integration chemical solution method, the test results indicate that the latter achieves 1.74 times acceleration performance than the former. Considering the TDAC method is utilized to speed up the chemical solution process at run-time, the comparison of computational efficiency between the TDAC method and the traditional direct stiff integration method is also performed for the preferred skeletal mechanism 26S–117R. Corresponding test results demonstrate that the former provides approximately 2.71 times acceleration performance compared to the latter. According to the above results, it can be further proved that the computational efficiency can be significantly improved by performing

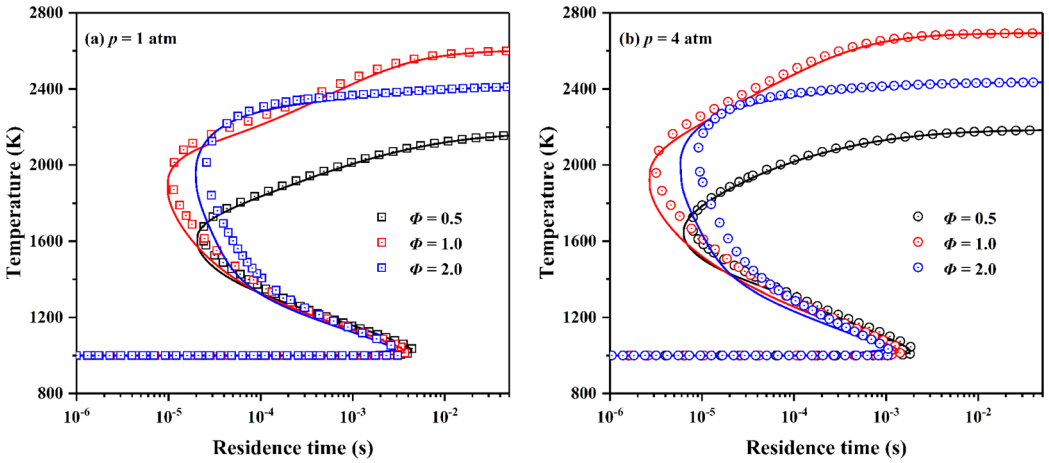

Fig. 7 "S"-curves of ethylene/vitiated air mixture in PSR simulated by different mechanisms at equivalence ratios of 0.5, 1.0 and 2.0 and pressures of 1 and 4 atm. Symbols are prediction using NUIGMech1.2; solid lines are prediction using the skeletal mechanism.

multi-stage integrated skeletal reduction and using the TDAC method. Thus, subsequent combustion simulations for the scramjet combustor adopt the skeletal mechanism 26S–117R of ethylene and the TDAC method. Two typical operating conditions of a scramjet mode and a ramjet mode are investigated to reveal their flow and combustion characteristics. The corresponding simulation results on reactive flow field against experimental measurements[10] of flame luminosity images, schlieren images, static pressure distribution profiles are presented in Fig. 8–10. Flame luminosity image can intuitively characterize the outline of combustion zones and serve for the flame stabilization mechanism analysis in scramjet combustors.[10,107,108] The flame luminosity is usually reflected by temperature contours in combustion simulation.[17,18] Fig. 8 illustrates the simulated temperature contours of the central cross-section for the two operating modes. Simulation results well characterize the combustion characteristics around the two cavities in both operating modes and match well with those of experimental measurements. The thermodynamic throats formed owing to combustion heat release are comparable to those observed in experiments. Besides, the spreading angles obtained from the simulations are in good agreement with the corresponding experimental measurements for the two operating modes. The flames near the T1 and B1 cavities are visually nearly identical for the scramjet mode, whereas significant differences are recognized between the two flames for the ramjet mode, with distinct flame upstream propagation observed near the T1 cavity. Wang *et al.*[109] summarized three

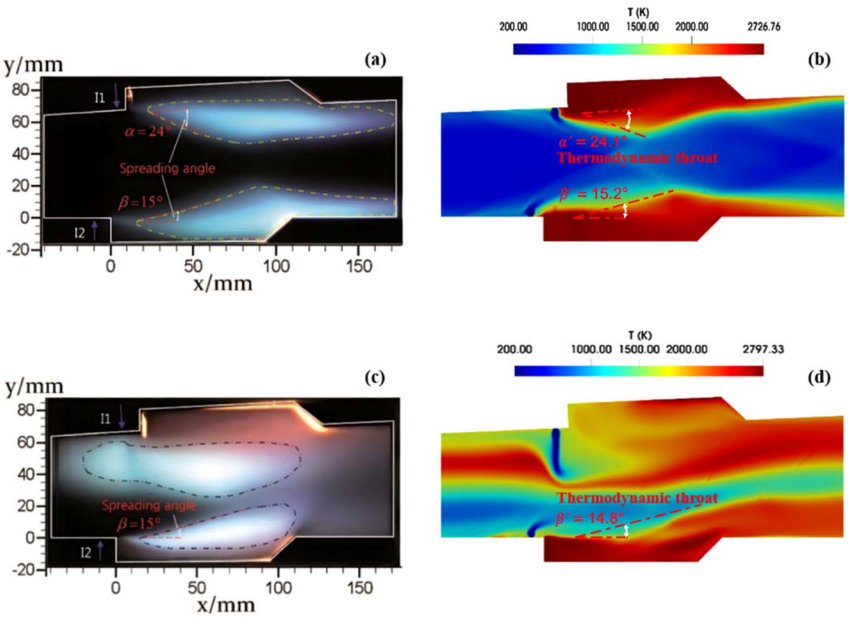

Fig. 8 The comparison between the experimental flame luminosity images (left column) and the numerical results (right column). (a) and (b) for the scramjet mode; (c) and (d) for the ramjet mode.

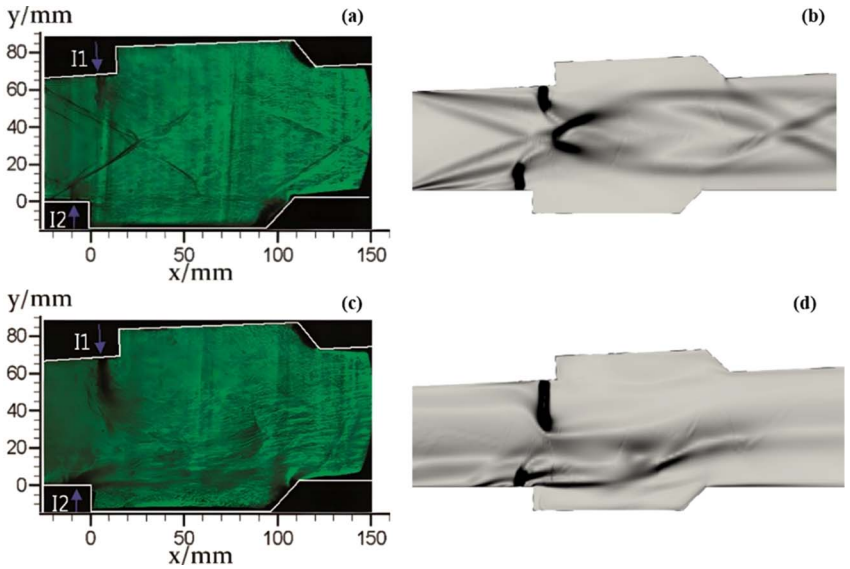

Fig. 9 The comparison of experimental measured schlieren images (left column) and numerical schlieren images (right column). (a) and (b) for the scramjet mode; (c) and (d) for the ramjet mode.

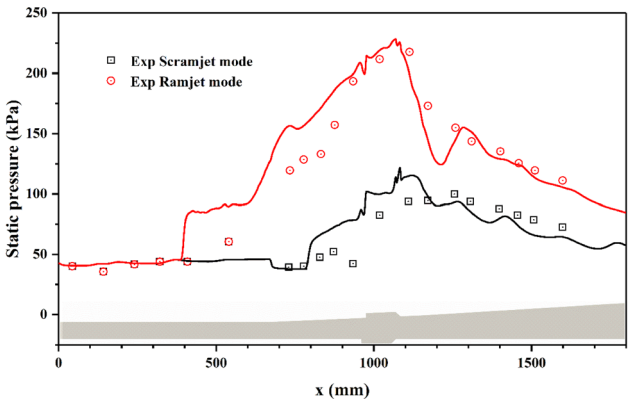

Fig. 10 The comparison of static pressure profiles for the two combustion modes. Symbols are experimental data; solid lines are simulated results.

different combustion stabilization mechanisms for cavity-based scramjet combustor based on optical observations. On the flames in both T1 and B1 cavities of the scramjet mode, the combustion stabilization attributes to cavity assisted jet-wake stabilized combustion. Whereas for the ramjet mode, the flames in T1 and B1 cavities respectively belong to combined cavity shear-layer/recirculation stabilized combustion and cavity shear-layer stabilized combustion.

Schlieren images are especially applicable to measuring density gradient in compressible flow fields, which can be used to capture shock and expansion waves, and turbulent structures in mixing and wake flows.[110] The numerical schlieren images (calculated by $|\nabla\rho|$) under the two operating modes are presented in Fig. 9 against corresponding experimentally measured images. In general, the numerical schlieren images well capture the complex structure of shock and expansion waves and their complex interaction with ethylene jets. For the scramjet mode as shown in Fig. 9(a) and (b), the heat release of combustion is quite small and the thermal blockage has minor effect on the mainstream. Pre-combustion shock waves is generated upstream of the two cavities due to the slightly flame upstream propagation and the formation of small recirculation zones ahead of the ethylene jets.[10] Since combustion occurs mainly in ethylene jet-wake and cavity, cavity shear layers are slightly curved towards the mainstream side. The shock waves are reflected between the shear layers with gradually decreasing intensity. For the ramjet mode as illustrated in Fig. 9(c) and (d), the increase of global equivalence ratio results in more heat release, and then has a greater effect on the mainstream. Due to the intense thermal blockage, the mainstream is significantly slowed down before entering the combustor and the pre-combustion shock waves shift forward. Meanwhile, the different flow characteristics presented by ethylene jets injected by the I1 and I2 injectors using the same injection pressure are well reproduced by the numerical schlieren images for both modes.

The static pressure profiles along the combustor directly reflect the intensity and distribution of combustion heat release.[10] Fig. 10 provides the simulated pressure profiles along the centreline of the upper wall for the two combustion modes. The simulated pressure profiles coincide well with the corresponding experimental measurements in terms of the initial pressure rise location and the pressure rise ratio. For the scramjet mode, the heat release intensity is low and the static pressure rise is mainly limited in T1 cavity and its downstream. Whereas for the ramjet mode, more intense and sufficient combustion around T1 cavity and its downstream causes the static pressure increased significantly. Consistent with Fig. 8(c), the high back pressure caused by intense heat release leads to

remarkable flame upstream propagation and the formation of recirculation zone in the upstream of T1 cavity.[10]

Above detailed comparison and discussion demonstrates that present combustion simulation obtains reliable results using the ethylene skeletal mechanism, which further illustrates the applicability of the skeletal mechanism derivate from the integrated reduction strategy. The corresponding files of kinetic, thermodynamic, and transport data for this mechanism are provided in the ESI.† To further demonstrate the advantage of this mechanism, the corresponding combustion simulation results of the skeletal mechanism 26S–117R are compared with those of other mechanisms in related works. Detailed comparisons and discussions, as given in the ESI,† demonstrate that present skeletal mechanism gives predictions more in line with corresponding experimental measurements. Based on the numerical simulation results, present work further analyses combustion performance parameters including combustion efficiency η_{comb},[93] total pressure loss $\eta_{p_{\mathrm{t,loss}}}$,[93] and net thrust ΔF,[12] which are difficult to measure experimentally but are important for combustor design. The definitions of these parameters are given by eqn (1)–(3).

$$\eta_{\mathrm{comb}} = \frac{1}{n}\sum_{1}^{n}\frac{\left[(1/\nu_{\mathrm{CO_2}})\int(A(x)(\rho u_x Y_{\mathrm{CO_2}}))\mathrm{d}A/W_{\mathrm{CO_2}}\right]_{\mathrm{inlet}}^{x}}{\dot{m}_{\mathrm{C_2H_4}}/W_{\mathrm{C_2H_4}}} \quad (1)$$

$$\eta_{p_{\mathrm{t,loss}}} = 1 - \frac{1}{n}\sum_{1}^{n}\frac{\int(A(x)\rho u_x p_{\mathrm{t},x})\mathrm{d}A}{\int(A(x)\rho u_x p_{\mathrm{t,inlet}})\mathrm{d}A} \quad (2)$$

$$\Delta F = \frac{1}{n}\sum_{1}^{n}\left[\int(A(x)(\rho u_x u_x + p))\mathrm{d}A\right]_{\mathrm{inlet}}^{x} \quad (3)$$

where ρ is gas density, u_x is streamwise velocity, p_{t} is the total pressure. $\nu_{\mathrm{CO_2}}$, $Y_{\mathrm{CO_2}}$ and $W_{\mathrm{CO_2}}$ are respectively stoichiometric coefficient, mass fraction and molecular weight of CO_2. $\dot{m}_{\mathrm{C_2H_4}}$ and $W_{\mathrm{C_2H_4}}$ are the mass flow rate and molecular weight of ethylene. The subscript "inlet" and superscript "x" respectively denotes inlet plane and different streamwise location. $A(x)$ represents that the cross-sectional area varies with different streamwise locations, and n is the number of time sequences.

Fig. 11 compares the combustion performance parameters of the two operating modes. For the scramjet mode, the combustion intensity is weak in the wake of ethylene jets and cavities. The combustion efficiency gradually increases as combustion proceeds in the near-wall region downstream of the parallel cavities. For the ramjet mode, the recirculation zone generated around the T1 cavity provides favourable combustion conditions, thus higher combustion efficiency is achieved near here. From x = 1800 mm, the combustion efficiency of the scramjet mode exceeds that of the ramjet mode, with a final value of 0.825 at the combustor outlet, higher than the corresponding value of 0.729 for the ramjet mode. This is attributed to the richer oxygen condition ensuring a more complete conversion of the fuel into final combustion products, whereas for the ramjet mode, intermediate products (*e.g.*, CO) are still abundantly exist until the combustor outlet. However, the final combustion efficiencies of the two modes are still insufficient and further method need to be taken to improve them. As for

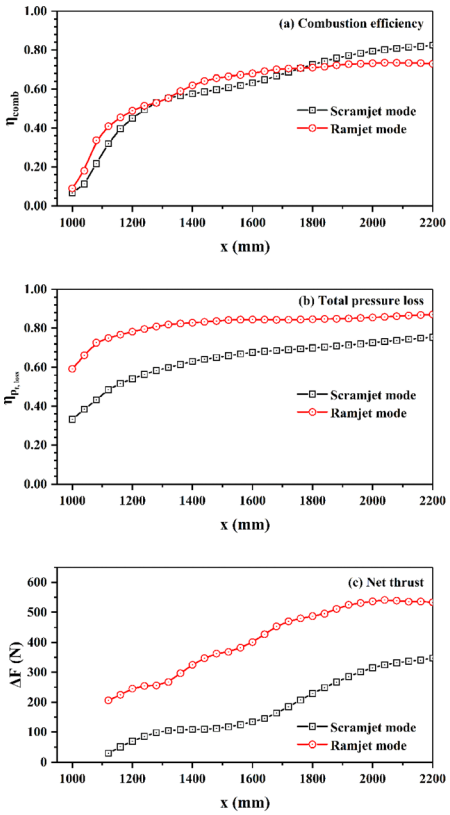

Fig. 11 The combustion efficiency (a), total pressure loss (b), and net thrust (c) for the two modes along the streamwise location.

the total pressure loss, the ramjet mode is in average 0.182 and in maximum 0.294 higher than that of the scramjet mode. There is more combustion heat release in the ramjet mode, thereby the corresponding Rayleigh heat loss leads to a greater total pressure loss.[93] The total pressure losses at the combustor outlet are respectively 0.753 and 0.871 for the scramjet and ramjet modes. The profiles of net thrust are calculated starting from the downstream of the two parallel cavities. As can be noted that the net thrust generated by the ramjet mode is higher than that of the scramjet mode, with final values of 533.3 N and 347.4 N at the combustor outlet, respectively.

4. Conclusions

Considering the lack of a high-fidelity ethylene skeletal mechanism suitable for combustion simulation of scramjet combustors, present work aims to obtain a compact and comprehensively validated ethylene skeletal mechanism qualified for wide combustion conditions. The static integrated skeletal reduction strategy successively consisting methods of r-DRGEP with FS scheme, improved SA and CSP importance index is performed for the hierarchically constructed NUIGMech1.2 under wide reduction conditions of temperature range of 900–1800 K, pressure range of 1–4 atm, and equivalence ratio range of 0.25–5.0. A skeletal mechanism 26S–117R with remarkably reduced size is obtained, and then it is comprehensively validated in terms of IDTs, LFSs, SCPs, AFTPs and "S"-curves. While the high-fidelity

skeletal mechanism is applied to the combustion simulations of the ethylene-fueled scramjet combustor with double parallel cavities, the PFA dynamic reduction method and ISAT algorithm of TDAC is adopted to further speed up the chemical reaction solution process at run-time. Under the scramjet and the ramjet mode, the corresponding simulation results of flame luminosity images, schlieren images, and static pressure distributions, coincide well with those of experimental measurements, which further demonstrates the applicability of the skeletal mechanism derivate from the integrated reduction strategy. According to combustion efficiency, total pressure loss, and net thrust, the effects of the two modes on combustion performance are quantitatively compared, which are important for combustor design. The integrated reduction strategy and systematic kinetic verification used in present work provide reference values for the application of fuel mechanisms in scramjet combustor combustion simulation.

Author contributions

Zhongwen Li: conceptualization, methodology, investigation, formalanalysis, writing – original draft. Jianwen Liu: methodology, writing – review & editing. Jingbo Wang: resources, conceptualization, funding acquisition, supervision, writing – review & editing.

Conflicts of interest

There are no conflicts to declare.

References

1 S. P. Zeppieri, S. D. Klotz and F. L. Dryer, *Proc. Combust. Inst.*, 2000, **28**, 1587–1595.
2 Q.-D. Wang, J.-B. Wang, J.-Q. Li, N.-X. Tan and X.-Y. Li, *Combust. Flame*, 2011, **158**, 217–226.
3 Z. Zhong, Z. Wang and M. Sun, *Acta Astronaut.*, 2015, **110**, 1–8.
4 N. Zettervall, C. Fureby and E. J. K. Nilsson, *Energy Fuels*, 2017, **31**, 14138–14149.
5 F. Zhong, L. Cheng, H. Gu and X. Zhang, *Aerosp. Sci. Technol.*, 2019, **86**, 775–781.
6 A. Brindle, R. Boyce and A. Neely, in *AIAA/CIRA 13th International Space Planes and Hypersonics Systems and Technologies Conference*, 2005, DOI: 10.2514/6.2005-3239.
7 G. L. Pellett, S. N. Vaden and L. G. Wilson, in *55th JANNAF Propulsion Meeting*, 2008.
8 X. J. Fan, F. Q. Zhong, G. Yu, J. G. Li and C. J. Sung, *J. Propul. Power*, 2009, **25**, 1226–1232.
9 K. Jackson, M. Gruber and T. Barhorst, *Presented in Part at the 45th AIAA/ASME/SAE/ASEE Joint Propulsion Conference & Exhibit*, Denver, Colorado, 2-5 August 2009.
10 Z. Zhong, Z. Wang, M. Sun and H. Wang, *Proc. Inst. Mech. Eng., Part G*, 2016, **230**, 2515–2522.
11 K. Wu, W. Yao and X. Fan, *Energy Fuels*, 2017, **31**, 14296–14305.
12 M. Dharavath, P. Manna and D. Chakraborty, *Acta Astronaut.*, 2015, **117**, 305–318.
13 M. Dharavath, P. Manna and D. Chakraborty, *Acta Astronaut.*, 2016, **128**, 107–118.
14 M. Mawid, B. Sekar, M. Mawid and B. Sekar, in *33rd Joint Propulsion Conference and Exhibit*, 1997.
15 C. K. Westbrook and F. L. Dryer, *Combust. Sci. Technol.*, 1981, **27**, 31–43.
16 Z. Cai, Z. Wang, M. Sun and X.-S. Bai, in *21st AIAA International Space Planes and Hypersonics Technologies Conference*, American Institute of Aeronautics and Astronautics, 2017.
17 T. Gao, J. Liang, M. Sun and Z. Zhong, *Proc. Inst. Mech. Eng., Part G*, 2017, **231**, 1862–1872.
18 M. B. Sun, Z. Zhong, T. Gao, H. Wang and J. Liang, in *21st AIAA International Space Planes and Hypersonics Technologies Conference*, 2017.
19 J. Liu, C. J. Tam, T. Lu and C. Law, in *42nd AIAA/ASME/SAE/ASEE Joint Propulsion Conference & Exhibit*, American Institute of Aeronautics and Astronautics, 2006.
20 C. K. Law, C. J. Sung, H. Wang and T. F. Lu, *AIAA J.*, 2003, **41**, 1629–1646.
21 A. Irannejad, A. Banaeizadeh and F. Jaberi, *Combust. Flame*, 2015, **162**, 431–450.
22 X. Liu, Z. Cai, Y. Tong and H. Zheng, *Acta Astronaut.*, 2017, **137**, 1–7.
23 H. Wang and A. Laskin, *Progress Report for an AFOSR New World Vista Program*, 1998.
24 N. M. Marinov, W. J. Pitz, C. K. Westbrook, A. M. Vincitore, M. J. Castaldi, S. M. Senkan and C. F. Melius, *Combust. Flame*, 1998, **114**, 192–213.
25 G. P. Smith, D. M. Golden, M. Frenklach, N. W. Moriarty, B. Eiteneer, M. Goldenberg, C. T. Bowman, R. K. Hanson, S. Song, W. C. Gardiner Jr, V. V. Lissianski and Z. Qin, *GRI3.0*, http://www.me.berkeley.edu/gri_mech/.
26 Z. Qin, V. V. Lissianski, H. Yang, W. C. Gardiner, S. G. Davis and H. Wang, *Proc. Combust. Inst.*, 2000, **28**, 1663–1669.
27 A. Konnov, *Eurasian Chem.-Technol. J.*, 2000, **2**, 257–264.
28 H. Wang, X. You, A. V. Joshi, S. G. Davis, A. Laskin, F. Egolfopoulos and C. K. Law, *UCS II*, http://ignis.usc.edu/USC_Mech_II.htm.
29 J. G. Lopez, C. L. Rasmussen, M. U. Alzueta, Y. Gao, P. Marshall and P. Glarborg, *Proc. Combust. Inst.*, 2009, **32**, 367–375.
30 C. Xu and A. A. Konnov, *Energy*, 2012, **43**, 19–29.
31 E. Ranzi, A. Frassoldati, R. Grana, A. Cuoci, T. Faravelli, A. P. Kelley and C. K. Law, *Prog. Energy Combust. Sci.*, 2012, **38**, 468–501.
32 *San Diego mechanism web page*, University of California, at, San Diego, http://combustion.ucsd.edu.
33 C.-W. Zhou, Y. Li, U. Burke, C. Banyon, K. P. Somers, S. Ding, S. Khan, J. W. Hargis, T. Sikes, O. Mathieu, E. L. Petersen, M. AlAbbad, A. Farooq, Y. Pan, Y. Zhang, Z. Huang, J. Lopez, Z. Loparo, S. S. Vasu and H. J. Curran, *Combust. Flame*, 2018, **197**, 423–438.
34 M. Yang, Z. Wan, N. Tan, C. Zhang, J. Wang and X. Li, *Combust. Flame*, 2020, **221**, 20–40.

35 M. Baigmohammadi, V. Patel, S. Martinez, S. Panigrahy, A. Ramalingam, U. Burke, K. P. Somers, K. A. Heufer, A. Pekalski and H. J. Curran, *Energy Fuels*, 2020, **34**, 3755–3771.
36 S. S. Nagaraja, J. Liang, S. Dong, S. Panigrahy, A. Sahu, G. Kukkadapu, S. W. Wagnon, W. J. Pitz and H. J. Curran, *Combust. Flame*, 2020, **219**, 456–466.
37 Y. Wu, S. Panigrahy, A. B. Sahu, C. Bariki, J. Beeckmann, J. Liang, A. A. E. Mohamed, S. Dong, C. Tang, H. Pitsch, Z. Huang and H. J. Curran, *Combust. Flame*, 2021, **226**, 229–242.
38 S. Martinez, M. Baigmohammadi, V. Patel, S. Panigrahy, A. B. Sahu, S. Nagaraja, A. Ramalingam, K. A. Heufer, A. Pekalski and H. J. Curran, *Combust. Flame*, 2021, **234**, 111626.
39 S. Dong, K. Zhang, P. K. Senecal, G. Kukkadapu, S. W. Wagnon, S. Barrett, N. Lokachari, S. Panigaphy, W. J. Pitz and H. J. Curran, *Proc. Combust. Inst.*, 2021, **38**, 611–619.
40 M. Baigmohammadi, V. Patel, S. Nagaraja, A. Ramalingam, S. Martinez, S. Panigrahy, A. A. E.-S. Mohamed, K. P. Somers, U. Burke, K. A. Heufer, A. Pekalski and H. J. Curran, *Energy Fuels*, 2020, **34**, 8808–8823.
41 S. Martinez, M. Baigmohammadi, V. Patel, S. Panigrahy, A. B. Sahu, S. S. Nagaraja, A. Ramalingam, A. A. E.-S. Mohamed, K. P. Somers, K. A. Heufer, A. Pekalski and H. J. Curran, *Combust. Flame*, 2021, **228**, 401–414.
42 T. Lu and C. K. Law, *Prog. Energy Combust. Sci.*, 2009, **35**, 192–215.
43 Z. Luo, C. S. Yoo, E. S. Richardson, J. H. Chen, C. K. Law and T. Lu, *Combust. Flame*, 2012, **159**, 265–274.
44 J. Xue, S. Xi and F. Wang, *Combust. Flame*, 2020, **214**, 184–198.
45 T. Lu and C. K. Law, *Proc. Combust. Inst.*, 2005, **30**, 1333–1341.
46 Z. Luo, T. Lu, M. J. Maciaszek, S. Som and D. E. Longman, *Energy Fuels*, 2010, **24**, 6283–6293.
47 P. Pepiot-Desjardins and H. Pitsch, *Combust. Flame*, 2008, **154**, 67–81.
48 W. Sun, Z. Chen, X. Gou and Y. Ju, *Combust. Flame*, 2010, **157**, 1298–1307.
49 Y. Wu, Y. Liu and T. Lu, *Combust. Flame*, 2020, **211**, 303–311.
50 X. L. Zheng, T. F. Lu and C. K. Law, *Proc. Combust. Inst.*, 2007, **31**, 367–375.
51 K. E. Niemeyer, C.-J. Sung and M. P. Raju, *Combust. Flame*, 2010, **157**, 1760–1770.
52 R. Li, S. Li, F. Wang and X. Li, *Combust. Flame*, 2016, **166**, 55–65.
53 S. Xi, J. Xue, F. Wang and X. Li, *Combust. Flame*, 2020, **222**, 326–335.
54 F. Karst, M. Maestri, H. Freund and K. Sundmacher, *Chem. Eng. J.*, 2015, **281**, 981–994.
55 T. Lu and C. K. Law, *Combust. Flame*, 2008, **154**, 153–163.
56 T. Lu and C. K. Law, *J. Phys. Chem. A*, 2006, **110**, 13202–13208.
57 T. Løvs, D. Nilsson and F. Mauss, *Proc. Combust. Inst.*, 2000, **28**, 1809–1815.
58 T. Lu, Y. Ju and C. K. Law, *Combust. Flame*, 2001, **126**, 1445–1455.
59 G. Xiao, *Energy Fuels*, 2020, **34**, 6367–6382.
60 R. Shan and T. Lu, *Combust. Flame*, 2012, **159**, 2069–2076.
61 F. Zhong, S. Ma, X. Zhang, C.-J. Sung and K. E. Niemeyer, *Acta Mech. Sin.*, 2015, **31**, 732–740.
62 B. Liu, F. Qin and D. Cao, in *51st AIAA/SAE/ASEE Joint Propulsion Conference*, 2015.
63 B. Liu, G.-Q. He and F. Qin, *Acta Astronaut.*, 2018, **152**, 521–533.
64 J. Li, L. Yuan, W. Li and K. Zhang, *Int. J. Aerosp. Eng.*, 2018, **2018**, 8672760.
65 J. He, J. Li, X. Ma, B. Meng and B. Tian, *Fuel*, 2023, **342**, 127812.
66 F. Contino, H. Jeanmart, T. Lucchini and G. D'Errico, *Proc. Combust. Inst.*, 2011, **33**, 3057–3064.
67 Z. Li, M. T. Lewandowski, F. Contino and A. Parente, *Energy Fuels*, 2018, **32**, 10121–10131.
68 K. Wu, F. Contino, W. Yao and X. Fan, *Combust. Flame*, 2018, **197**, 265–275.
69 J. An, G. He, F. Qin, X. Wei and B. Liu, *Combust. Flame*, 2019, **206**, 467–475.
70 S. B. Pope, *Combust. Theory Modell.*, 1997, **1**, 41–63.
71 L. Liang, J. G. Stevens and J. T. Farrell, *Proc. Combust. Inst.*, 2009, **32**, 527–534.
72 Y. L. Ong, F. Salehi, M. Ghiji and V. Garaniya, *Combust. Theory Modell.*, 2021, **25**, 208–234.
73 A. Storch, M. Bynum, J. Liu and M. Gruber, in *17th AIAA International Space Planes and Hypersonic Systems and Technologies Conference*, 2011.
74 *Chemkin-pro 15112, Reaction Design*, San Diego, 2011.
75 S. H. Li, J. W. Liu, R. Li, F. Wang and X. Y. Li, *Chem. J. Chin. Univ.*, 2015, **36**, 1576–1587.
76 Z. Tian, J. Li and Y. Yan, *Fuel*, 2019, **250**, 52–64.
77 J. W. Jung, Y. C. Lim and H. K. Suh, *Proc. Inst. Mech. Eng., Part D*, 2020, **234**, 3398–3413.
78 D. J. Micka, *Combustion stabilization, structure, and spreading in a laboratory dual-mode scramjet combustor*, University of Michigan, 2010.
79 Z. Li, J. Wang and X. Li, *Fuel*, 2023, **349**, 128659.
80 *OpenFOAM*, **https://openfoam.org/**.
81 A. Kurganov and E. Tadmor, *J. Comput. Phys.*, 2000, **160**, 241–282.
82 C. J. Greenshields, H. G. Weller, L. Gasparini and J. M. Reese, *Int. J. Numer. Methods Fluids*, 2010, **63**, 1–21.
83 H. Zhang, M. Zhao and Z. Huang, *Fuel*, 2020, **282**, 118812.
84 B. van Leer, *J. Comput. Phys.*, 1974, **14**, 361–370.
85 F. Menter and T. Esch, in *16th Brazilian Congress of Mechanical Engineering (COBEM)*, 2001.
86 F. R. Menter, M. Kuntz and R. Langtry, *Turbul., Heat Mass Transfer*, 2003, **4**, 625–632.
87 *The OpenFOAM Foundation, kOmegaSSTBase*, **https://cpp.openfoam.org/v9/kOmegaSSTBase_8C_source.html**.
88 J. Chomiak and A. Karlsson, *Symp. (Int.) Combust.*, 1996, **26**, 2557–2564.

89 L. A. Vulis, *Thermal Regimes of Combustion*, McGraw-Hill, 1961.
90 V. I. Golovitchev, N. Nordin, R. Jarnicki and J. Chomiak, *SAE Trans.*, 2000, **109**, 1391–1405.
91 S. Zheng, H. Liu, R. Sui, B. Zhou and Q. Lu, *Combust. Flame*, 2022, **235**, 111699.
92 S. Zheng, Y. He, H. Liu, Y. Yang, W. Han and Q. Lu, *Int. J. Hydrogen Energy*, 2024, **49**, 1336–1345.
93 W. Yao, Y. Lu, K. Wu, J. Wang and X. Fan, *J. Propul. Power*, 2018, **34**, 975–991.
94 Z.-W. Huang, G.-Q. He, F. Qin and X.-G. Wei, *Int. J. Hydrogen Energy*, 2015, **40**, 9815–9824.
95 D. J. Micka and J. F. Driscoll, *Combust. Flame*, 2012, **159**, 1205–1214.
96 M. M. Kopp, N. S. Donato, E. L. Petersen, W. K. Metcalfe, S. M. Burke and H. J. Curran, *J. Propul. Power*, 2014, **30**, 790–798.
97 K. Wang, R. Xu, T. Parise, J. Shao, A. Movaghar, D. J. Lee, J.-W. Park, Y. Gao, T. Lu, F. N. Egolfopoulos, D. F. Davidson, R. K. Hanson, C. T. Bowman and H. Wang, *Combust. Flame*, 2018, **198**, 477–489.
98 O. Park, P. S. Veloo and F. N. Egolfopoulos, *Proc. Combust. Inst.*, 2013, **34**, 711–718.
99 G. Jomaas, X. L. Zheng, D. L. Zhu and C. K. Law, *Proc. Combust. Inst.*, 2005, **30**, 193–200.
100 T. Hirasawa, C. J. Sung, A. Joshi, Z. Yang, H. Wang and C. K. Law, *Proc. Combust. Inst.*, 2002, **29**, 1427–1434.
101 F. N. Egolfopoulos, D. L. Zhu and C. K. Law, *Symp. (Int.) Combust.*, 1991, **23**, 471–478.
102 M. I. Hassan, K. T. Aung, O. C. Kwon and G. M. Faeth, *J. Propul. Power*, 1998, **14**, 479–488.
103 K. Kumar, G. Mittal, C.-J. Sung and C. K. Law, *Combust. Flame*, 2008, **153**, 343–354.
104 S. Jallais, L. Bonneau, M. Auzanneau, V. Naudet and S. Bockel-Macal, *Ind. Eng. Chem. Res.*, 2002, **41**, 5659–5667.
105 M. Aliyu, A. Abdelhafez, M. A. Nemitallah, S. A. M. Said and M. A. Habib, *Energy*, 2022, **243**, 123077.
106 A. Abdelhafez, M. A. Nemitallah, S. S. Rashwan and M. A. Habib, *Energy Fuels*, 2018, **32**, 7868–7877.
107 Y. Tian, S. Yang, J. Le, T. Su, M. Yue, F. Zhong and X. Tian, *Int. J. Hydrogen Energy*, 2016, **41**, 19218–19230.
108 D. J. Micka and J. F. Driscoll, *Proc. Combust. Inst.*, 2009, **32**, 2397–2404.
109 H. Wang, Z. Wang, M. Sun and H. Wu, *Int. J. Hydrogen Energy*, 2013, **38**, 12078–12089.
110 T. Kouchi, C. P. Goyne, R. D. Rockwell and J. C. McDaniel, *Exp. Fluids*, 2015, **56**, 211.